Proceedings of the 9th World Congress on Momentum, Heat and Mass Transfer (MHMT 2024)
London, United Kingdom – April 11 – 13, 2024
Paper No. ICMFHT 148
DOI: 10.1115/icmfht24.148

Numerical Simulation of Liquid Film Evaporation and Condensation for Water Reactors

Yu Xia[1]
[1]Ansys UK Ltd.,
Milton Park, Abingdon, United Kingdom
steven.xia@ansys.com
Amine Ben Hadj Ali[2],
[2]Ansys Germany GmbH,
Schulze-Delitzsch-Str. 16, Stuttgart, Germany
amine.benhadjali@ansys.com
Alok Khaware[3]*
[3]Ansys Software Pvt Ltd,
Rajiv Gandhi Infotech Park, Pune, India
alok.khaware@ansys.com
Jing Cao[4]
[4]Ansys UK Ltd,
St Paul's Place, Sheffield, United Kingdom
jing.cao@ansys.com

Abstract – A detailed analysis of liquid film evaporation and condensation has become increasingly important, especially in water reactor designs. For example, the prediction of liquid film evaporation is critical to the design of Passive Containment Cooling Systems (PCCS), which are important passive safety facilities in modern Pressurized Water Reactors (PWR). To keep the maximum design values of pressure and temperature under control, a water/air counter-current flow is often employed within the external channel of the PCCS. It is thus essential to analyse the evaporation mass flow rate and heat transfer of the water film for the overall performance of PCCS. On the other hand, hydrogen might be released into the reactor containment during an incident due to cladding oxidation at elevated temperatures. Given the high flammability of gaseous hydrogen, it is paramount to know its local distribution in the containment building while considering wall condensation, which will increase the non-condensable gas concentration on the walls.

Another example is evaluating the containment loads in the Light Water Reactor (LWR) plants and predicting their condensation behaviour in the presence of non-condensable gases. With the advantages of Computational Fluid Dynamics (CFD) and recent model developments, the numerical analysis of evaporation and condensation of liquid films has become more convenient than expensive experiments for real-world applications. In this paper, the numerical model of Eulerian Wall Film (EWF) implemented within Ansys Fluent® has been validated based on two canonical cases. The first one refers to the experiments performed by Hu et al. [1], where the heat transfer during the water film evaporation on a vertical plate has been studied. The average heat flux and water film evaporative ratio match the available experimental data well. The second case relates to the experiments done by Ambrosini et al. [2], also known as the "CONAN" case, where the wall film condensation in the presence of non-condensable substances has been studied under different steam mass fraction and velocity conditions. The surface heat flux and condensate mass flow rate also match the experimental measurements. The present numerical workflow using EWF could be applied to more complex devices for liquid film evaporation and condensation simulations.

***Keywords*:** Eulerian Wall Film, Passive Containment Cooling System, Liquid Film Evaporation, Liquid Film Condensation

1. Introduction

The safety of a nuclear reactor is of utmost concern. Many passive safety facilities have been introduced into large-scale, advanced pressurized water reactors. For example, a Passive Containment Cooling System (PCCS) has been used in CAP1400 [3], AP600 [4], and AP1000 [5] reactors to remove the decay heat from the postulated accident scenarios. The actual heat removal capacity of a PCCS cooling system needs to be accurately calculated to control the safety criteria of a

Please address all correspondence to Alok Khaware (alok.khaware@ansys.com)

reactor. In a PCCS system, a gravity-driven water film usually flows downwards along the outer surface of the containment wall, with a counter-current buoyancy-driven air flow flowing upwards above the water film in the annular channel. The water film that evenly covers the heated shell wall would cool down the containment unit and the naturally circulating airflow, and the water film evaporation would dominate the heat transfer process. On the other hand, a large amount of steam may be released into the nuclear containment during a postulated Loss of Coolant Accident (LOCA). Using condensation on the containment walls has been considered one of the dominant passive mechanisms to maintain the pressure level below the designed threshold.

Computational Fluid Dynamics (CFD) has increased drastically for design and optimization purposes, mainly due to its capability to describe the flow patterns and the chemical component distributions in complex geometries such as nuclear reactors. The accurate modeling of evaporation and condensation plays an essential role in designing and testing PCCS systems. The complications involved in applying CFD to heat and mass transfer calculations have been very challenging, especially in the near-wall region. For example, predicting boundary layer behaviour is difficult for turbulent flows [6, 7], and it becomes more challenging when simulating the heat and mass transfer processes because the flow, thermal, and concentration boundary layers all superimpose and interact with each other.

Several studies have been performed to predict water film evaporation and condensation using different CFD codes. Xiao et al. [8] developed a dynamic water film model in a 3-D GASFLOW-MPI code by adding essential interphase exchange source terms in the mass, momentum, and energy governing equations. They found that the code could efficiently analyse the heat removal capacity of a PCCS unit. Hong et al. [9] used the Lee model implemented within Ansys Fluent® [10] to predict the characteristics of water evaporation heat transfer. Also, within Ansys Fluent®, Wang et al. [5] used the Eulerian Wall Film (EWF) model coupled with the Eulerian multiphase flow and species transport models to analyse the external cooling of the AP1000 PCCS system. Zschaeck et al. [11] performed several validation studies on wall condensation using Ansys CFD®, where the numerical model employs a mass sink on the isothermal walls. In the present study, the wall film evaporation and condensation have been analysed individually based on two canonical cases with experimental data, and the comparison between numerical and experimental results will be conducted and discussed.

2. Governing Equations – Eulerian Wall Film

The film governing equations are the results of depth-averaged N-S equations with the presumption of a thin film, where the film thickness is much smaller than the lateral dimensions of the physical surfaces and the film state variables are not resolved across the film thickness. Instead, prescribed film velocity and temperature profiles are employed, resulting in mean film state variables being solved.

The Fluent® built-in Eulerian Wall Film (EWF) model has been used in this work. The conservation equation of mass for a 2-D liquid film in a 3-D domain is given as:

$$\frac{\partial \rho_l h}{\partial t} + \nabla_s . \left(\rho_l h \vec{V}_l\right) = \dot{m}_s \tag{1}$$

where ρ_l is the liquid density, h the film height, ∇_s the surface operator, $\vec{V}_l$ the mean film velocity, and $\dot{m}_s$ the mass source per unit wall area due to droplet collection, film separation, film stripping, and phase change. The conservation equation of the film momentum is also defined as:

$$\frac{\partial \rho_l h \vec{V}_l}{\partial t} + \nabla_s . \left(\rho_l h \vec{V}_l \vec{V}_l + \bar{\bar{D}}_V\right) = - h \nabla_s \mathrm{P}_L + \rho_l h \vec{g}_\tau + \frac{2}{3} \vec{\tau}_{fs} - \frac{3\mu_l}{h} \vec{V}_l + \dot{\vec{q}}_s + \vec{\tau}_{\theta_w} \tag{2}$$

where:

$$\mathrm{P}_L = \mathrm{P}_{\mathrm{gas}} + \mathrm{P}_h + \mathrm{P}_\sigma \tag{3}$$

$$\mathrm{P}_h = -\rho h (\vec{n} . \vec{g}) \tag{4}$$

$$\mathrm{P}_\sigma = -\sigma \nabla_s . (\nabla_s h) \tag{5}$$

The two terms on the left-hand side of Eq. (2) represent transient and convection effects, respectively, with tensor $\overline{\overline{D}}_V$ denoting the differential advection term computed based on the prescribed film velocity profile. On the right-hand side of Eq. (2), the first term includes the effects of gas-flow pressure, the gravity component normal to the wall surface (known as "spreading"), and surface tension. The second term represents the effect of gravity in the direction parallel to the film. The third and fourth terms refer to the net viscous shear forces on the gas-film interface and the film-wall interface, respectively. The fifth term is associated with droplet collection or separation. The last term denotes the surface force based on the film's surface tension and contact angle. Please note that in arriving at the shear and viscous terms on the right-hand side of Eq. (2), a quadratic film velocity profile has been assumed.

The conservation equation of the film energy is finally as follows:

$$\frac{\partial \rho_l h T_f}{\partial t} \nabla_s \cdot \left(\rho_l h T_f \vec{V}_l + \vec{D}_T\right) = \frac{1}{C_p}\left[\frac{2k_f}{h}\left(T_s + T_w - 2T_m\right) + \dot{q}_{\text{imp}} + \dot{m}_{\text{vap}} L\right] \tag{6}$$

where T_f is the average film temperature, and vector $\vec{D}_T$ is the differential advection term computed using quadratic film velocity and temperature profiles. On the right-hand side of Eq. (6), the first term inside the bracket represents the net heat flux on the gas-film and film-wall interfaces, with T_s and T_w the film surface and wall temperatures, respectively. T_m is the film half depth temperature. All these temperatures have been computed based on the film's temperature profile and the thermal boundary conditions at gas-film and film-wall interfaces. $\dot{q}_{\text{imp}}$ denotes the source term due to liquid impingement from the bulk flow on the wall. $\dot{m}_{\text{vap}}$ is the mass vaporization or condensation rate, and L denotes the latent heat associated with the phase change.

The Eulerian wall film model can be coupled with the mixture species transport model to consider phase changes between film material (liquid) and the gas species (vapor). The rate of phase change is governed by,

$$\dot{m}_{\text{phase}} = \rho k_{\text{film}} \ln\left[\frac{1-Y_i}{1-Y_{\text{is}}}\right] \tag{7}$$

where ρ is density of the gas mixture, Y_i is the mass fraction of the condensable specie i, Y_{is} is the mass fraction of the condensable specie i at the film surface, and k_{film} is the mass transfer coefficient determined by the turbulent wall functions. The interfacial mass fraction, Y_{is}, is computed by assuming that the vapour is at the thermal equilibrium state with the liquid film. Therefore, the vapour's partial pressure in the gaseous mixture is equal to its saturation pressure at the film surface temperature. More details about the EWF model and the phase change models used in this work could be found in Ansys Fluent® Theory Guide [10].

Compared to a conventional wall condensation model, e.g., Ref. [11], which usually focuses on the condensation only and models the mass and energy source terms on the wall assuming the film is static and not modelling the details of the liquid film itself, the present EWF model covers both film condensation and evaporation, solving the transport equations of mass, momentum, and energy simultaneously. The wall condensation model assumes that the gas mixture saturates on the wall, while EWF treats the gas mixture saturation on the film surface.

3. Test Case I - Liquid Film Evaporation

3.1. Case Description

The first simulation case features a liquid film evaporation process. The main objective is to validate the Eulerian Wall Film model implemented in Ansys Fluent® for evaporation under wall heating. Simulation results have been compared to the experiments performed by Hu et al. [1]. The computational domain features a rectangular channel of L (5 m) × W (1.2 m) × H (0.3 m) with a steel plate on the bottom, as shown in Fig. 1. In this work, the channel is tilted at θ = 90° only, leading to a vertical channel. A water film of thickness δ = 0.01 m and width W = 1.2 m enters the domain through a top inlet and is adjacent to the bottom wall, which freely flows down under the impact of gravity. A counter-current airflow above the

water film travels upwards from a bottom inlet. The bottom steel plate has a uniform and fixed temperature, with the other walls being adiabatic. The velocity inlet condition is defined for both the airflow and the water film entries, where the velocity is normal to the inlet plane and has uniform speed and temperature profiles. Since the channel is open to the atmosphere, the pressure outlet condition is applied for airflow and water film outlets. The key boundary conditions are listed in Table 1.

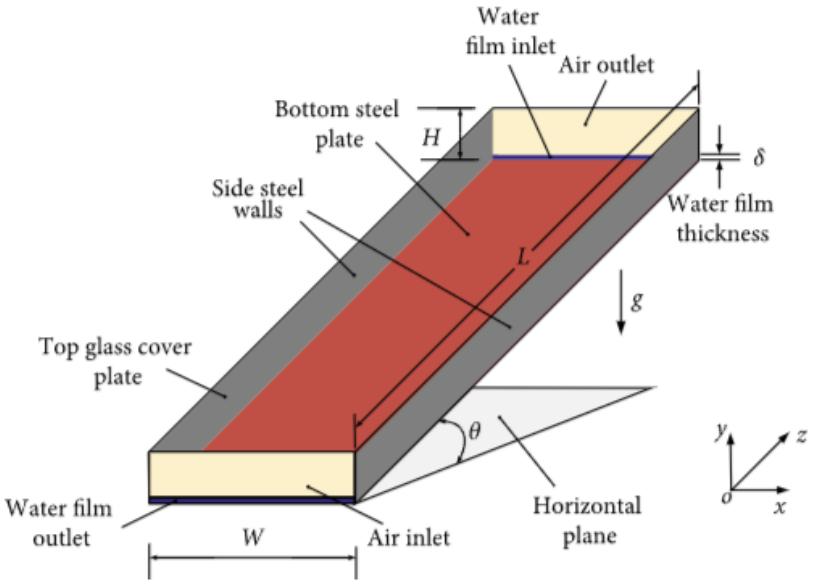

Figure 1. Schematic diagram of the computational domain. Image taken from Ref. [1].

Table 1. Key boundary conditions of the computational domain

Bottom wall temperature (℃)	Water film inlet temperature (℃)	Air inlet temperature (℃)	Air inlet velocity (m/s)	Water film inlet mass flow rate (kg/s)	Air inlet relative humidity (%)
84.72	70	44.59	2	0.18	36.0

3.2. Mesh Resolutions

Three hexahedral mesh grids have been created for the 3D domain to analyse mesh sensitivity. The mesh cell sizes, and total cell counts are listed in Table 2. All the meshes are structural and have a uniform resolution along the channel length (L) and width (W). Mesh A and Mesh B have the same numbers of cells in all directions, giving a total cell count of 0.96 million, while Mesh C has 1.5 times more cells than Meshes A and B in all three directions, leading to a total cell count of 3.24 million.

For the mesh resolutions along the channel height (H), especially near the bottom wall, Figure 2 compares the three meshes. Mesh A has a uniform cell height of 0.5 mm along the entire channel height. Meshes B and C have a non-uniform cell height distribution along the channel height, with a smaller first layer height of 0.1 mm on the bottom wall. Besides, Mesh C has more cells (90) along the channel height than Mesh B (60). Therefore, the impact of first layer height on the solutions can be evaluated by comparing Meshes A and B, while the influence of global mesh resolution on the simulations can be analysed by comparing Meshes B and C.

Table 2. Mesh resolutions and cell sizes

Mesh	Numbers of cells [-]: $L \times W \times H$	First layer height on bottom wall [mm]	Total cell count [-]
A	$200 \times 80 \times 60$	0.5	0.96 million
B	$200 \times 80 \times 60$	0.1	0.96 million
C	$300 \times 120 \times 90$	0.1	3.24 million

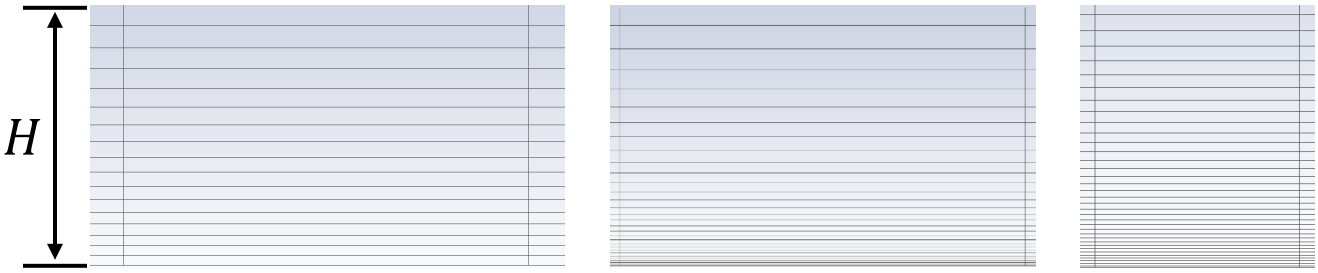

(a) Mesh A (b) Mesh B (c) Mesh C

Figure 2. Mesh resolutions along the channel height, H.

3.3. Numerical Settings

In this evaporation case, transient RANS simulations have been performed using the $k-\omega$ SST turbulence model to simulate the evolutions of film thickness, evaporative mass, surface heat transfer, etc. The ideal gas assumption and mixing law have been applied to the air/water vapor mixture. For the spatial discretization, the Second Order Upwind scheme has been used for mass, momentum, energy, and species mass fractions. The Bounded Second Order Upwind scheme is used for temporal formulation. All the simulations have been run sufficiently long until full convergence, using a fixed time step of 2.5×10^{-5} s, with 20 sub-iterations per time-step.

For the EWF model, momentum is solved with spreading and surface tension terms. The wall boundary layer model computes the phase change between liquid and vapor states. The film initial and boundary conditions include a maximum film thickness of 0.1 m, an initial film thickness of 0.01 m, an inflow mass flux, and an axial momentum flux computed based on Ref. [1], all of which have been used as inputs for the EWF model. The High Order Explicit scheme is used for temporal discretization within EWF, while the Second Order Upwind method is applied for continuity, momentum, and energy equations for EWF. The Coupled Solution has been used for the continuity-momentum coupling. An adaptive time-stepping is used within the EWF model, with a maximum Courant number of 0.1, an initial time step of 0.001s, an increase factor of 1.2, and a decrease factor of 2. More details of the implemented EWF model can be found in Ref. [10].

As shown in Fig. 3, the different EWF setups on the bottom wall have been explained. The bottom wall has been divided into three sections: the first section, marked as red, is at the film inlet and has EWF model disabled; the second section (marked as blue) has EWF enabled but no phase model; the majority of the bottom wall up to the film outlet is defined as the third section and marked as grey, which has the wall boundary layer phase change model enabled for EWF.

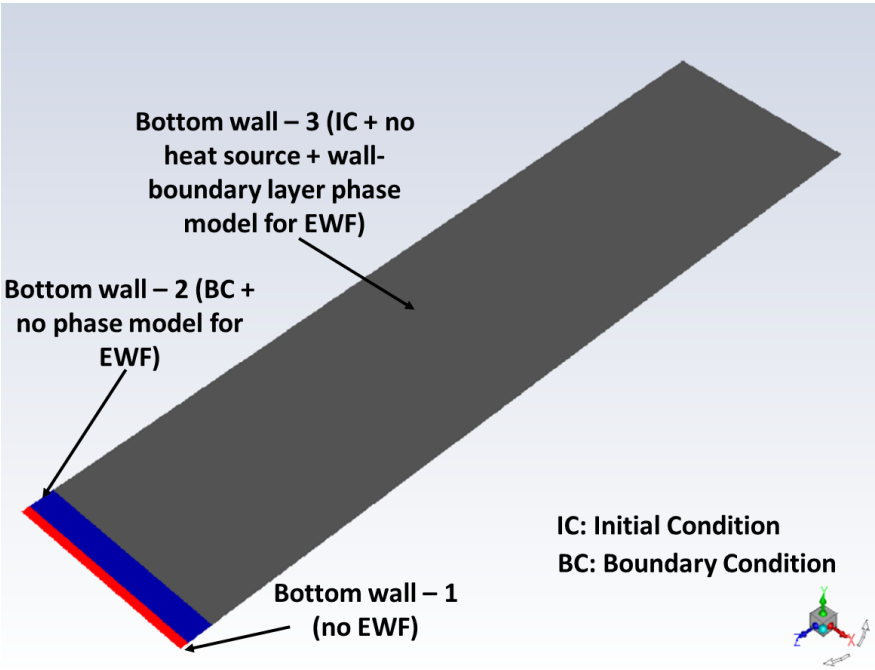

Figure 3. Different boundary conditions and EWF model setups on the bottom wall.

3.4. Results and Discussion

In this work, the default EWF model built within Fluent® 2022R2 has been used for all the simulations. The mesh sensitivity analysis is first performed using the total average heat flux ($q_{\omega,\text{ave,numerical}}$) and the water film evaporative ratio ($\omega_{\text{numerical}}$) computed on the bottom wall. ω is defined as the ratio of the water film evaporative mass flow rate to the water inflow mass flow rate. The three meshes A – C listed in Table 2 have been compared. As shown in Table 3, both the first layer height (Mesh A vs. B) and the cell sizes (Mesh B vs. C) have very limited impact (< 4%) on the simulation results. Therefore, a relatively coarse mesh (e.g., Mesh A) has been used for the following simulations.

Table 3. Total average heat fluxes and water film evaporative ratios for all three meshes.

Mesh	Average Heat Flux ($q_{\omega,\text{ave,numerical}}$) [kw/m^2]	Difference [%]	Water film evaporative ratio ($\omega_{\text{numerical}}$) [%]	Difference [%]
A	7.882	--	5.429	--
B	7.767	-1.47	5.246	-3.37
C	7.730	-1.93	5.267	-2.98

The simulation results of the total average heat flux ($q_{\omega,\text{ave,numerical}}$), and the water film evaporative ratio ($\omega_{\text{numerical}}$) on the bottom wall, have both been validated against the experimental data by Hu et al. [1] and a previous numerical study using a tuned EWF model and Fluent® 15.0 by Du et al. [13]. This tuned model calibrated the phase change coefficients.

It can be observed from Fig. 4 that the current predictions of $q_{\omega,\text{ave,numerical}}$ are less than $\pm 20\%$ different from the experiments, and they have a similar accuracy as those simulated by a tuned phase change model in Ref. [13].

For the film evaporative ratio, $\omega_{\text{numerical}}$, the present solutions are about 30% underpredicted compared to the measurement data [1], which may still be acceptable given the inbuilt EWF model does not tune any phase change coefficients. Further investigations are now underway to improve the prediction accuracy of the inbuilt EWF model.

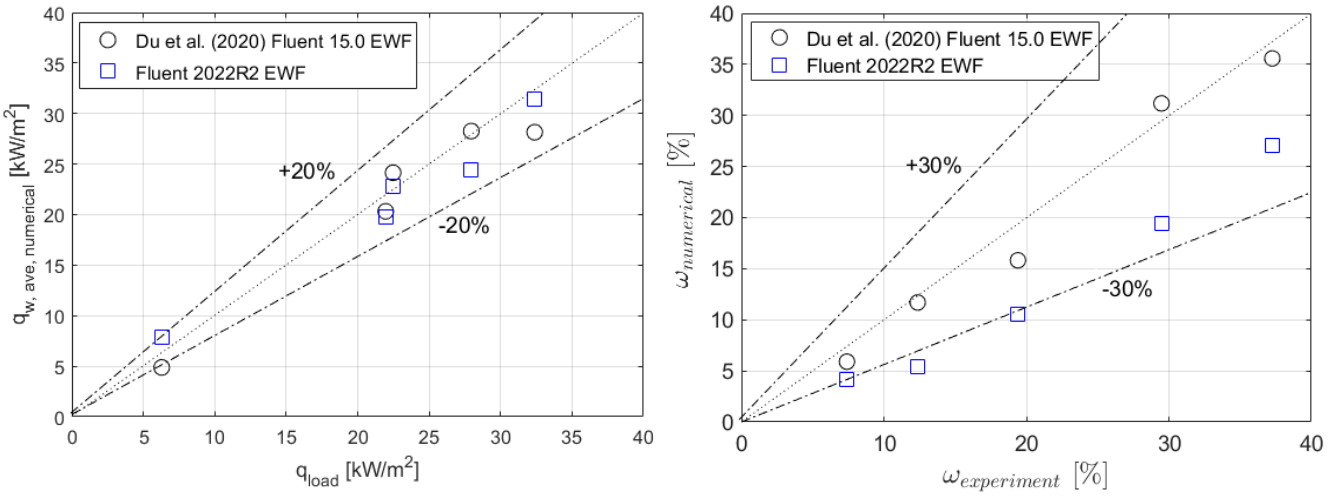

(a) (b)

Figure 4. The present simulated total average heat flux, $q_{\omega,\text{ave,numerical}}$, and water film evaporative ratio, $\omega_{\text{numerical}}$, comparing to experimental data by Hu et al. [1] (q_{load} and $\omega_{\text{experiment}}$) and tuned EWF simulations by Du et al. [13].

4. Test Case II - Liquid Film Condensation

4.1. Case Description

The second validation case, known as CONAN, focuses on liquid film condensation, again using the EWF model built within Fluent® 2022R1. The relevant experiments have been performed by Ambrosini et al. [2, 14], as shown in Fig. 5(a), which feature: (1) a vertical square duct, known as the "Primary Test Channel" (in red colour), in which a mixture of air and water vapour flows downwards while being cooled on a wall made of a 4.5 cm thick aluminium plate (in green colour). The rear side of this metal plate is cooled by the liquid water flowing upwards in a rectangular duct called a "Secondary Coolant Channel" (in blue colour). The Primary Test Channel has a length of 2 m and a width or depth of 0.34 m, whereas the Secondary Coolant Channel has a length of 2 m, a width of 0.35 m, and a small depth of 0.005 m. The mixture of water vapor (or "steam") and air enters the domain through the primary channel's top end. In contrast, the liquid water (or "coolant") enters via the secondary channel's bottom surface. In this work, the computational domain used by the simulations (see Fig. 5(b)) refers to a narrow slice of the experimental facility in the vertical z-direction, which applies symmetry conditions on the domain side boundaries. The surface heat fluxes and the condensate mass flow rates along the plate's centreline have been computed for several operating points and compared with the available experimental data.

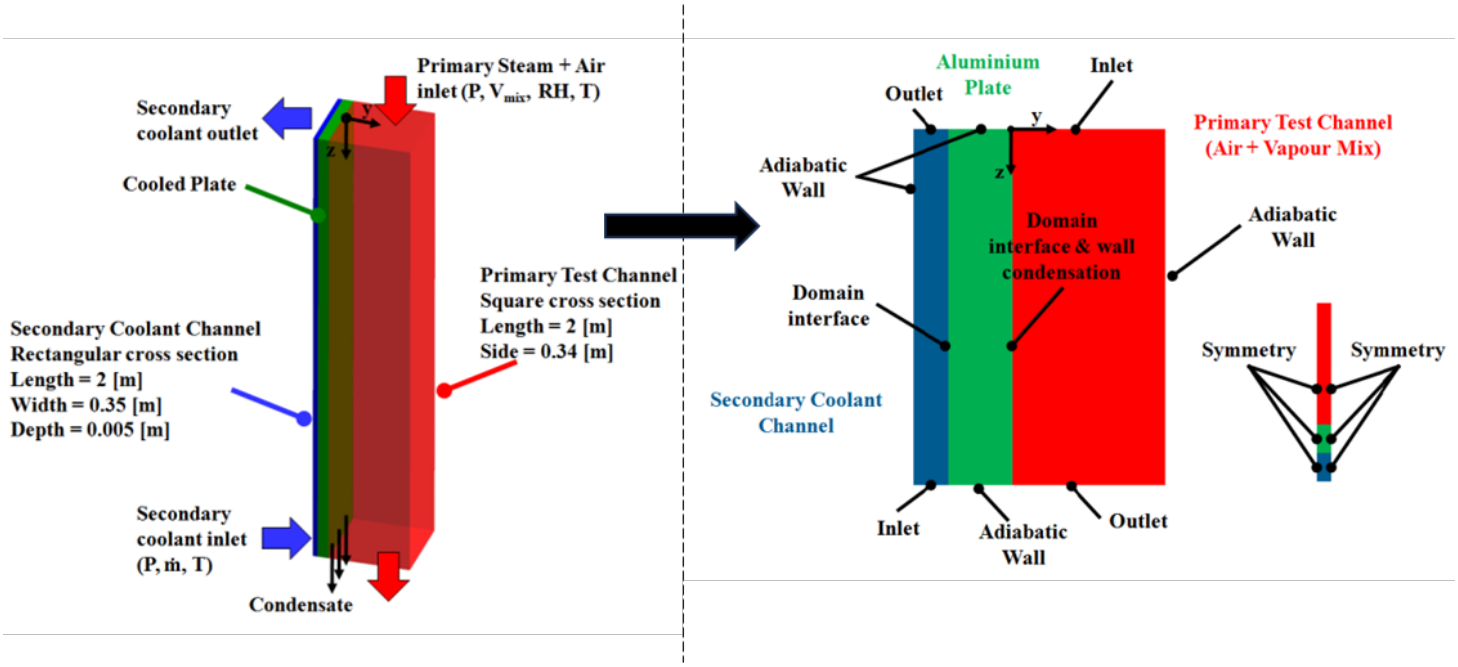

Figure 5. Schematic diagram of the CONAN (a) experimental facility and (b) computational domain [2, 11]

4.2. Operating and Boundary Conditions

For this condensation case, five different operating conditions have been simulated with different inlet conditions for both primary and secondary channels, as listed in Table 4. T denotes temperature, $\dot{m}$ the mass flow rate, V the velocity, and φ the relative humidity. The subscript "in" means inlet, "water" the liquid water, and "mix" the air/water-vapor mixture.

Table 4. Inlet conditions of the computational domain for different cases

No.	Case Name	Secondary Coolant Channel (liquid water)		Primary Test Channel (air/water-vapor mixture)		
		$T_{\text{in,water}}$ [°C]	$\dot{m}_{\text{in,water}}$ [kg/s]	$V_{\text{in,mix}}$ [m/s]	$\varphi_{\text{in,mix}}$ [%]	$T_{\text{in,mix}}$ [°C]
1	P10-T30-V15	31.24	1.217080	1.46	100.00	82.66
2	P10-T30-V20	31.10	1.217269	2.02	100.00	80.61
3	P10-T30-V25	31.07	1.216775	2.52	97.83	79.13
4	P10-T30-V30	30.91	1.216021	3.01	87.35	78.73
5	P10-T30-V35	30.71	1.215940	3.59	96.55	75.02

4.3. Mesh Resolutions

The mesh sensitivity analysis was also performed using a series of five hexahedral mesh grids, as defined in Table 5. Simulation results such as condensate mass flow rate and surface heat flux have been compared across different mesh refinement levels to evaluate the dependence of solution accuracy on the mesh resolution.

Table 5. Mesh resolutions and cell sizes

Mesh No.	No. of Nodes	No. of Elements	Maximum Aspect Ratio	Average Y+
1	13,630	6,404	101.7	6.70
2	45,824	22,145	217.3	2.02
3	220,448	108,660	533.6	0.39
4	783,894	388,363	517.6	0.22
5	3,551,588	1,765,928	1090.0	0.11

4.4. Numerical Settings

For this CONAN case, steady-state RANS simulations have been performed using the k-ω SST turbulence model to predict the final film thickness, condensation mass and surface heat transfer, etc. Same as the above film evaporation case (see Sec. 3), the ideal gas assumption and mixing law have been applied for the air/water vapor mixture. The Coupled scheme is used for pressure-velocity coupling, with the pseudo transient model being enabled. The Second Order Upwind method has been utilized for mass, momentum, energy, and species mass fractions, after comparing to the first order simulation results. The Conjugate Heat Transfer (CHT) model has also been applied to model both the solid and fluid domains, with fixed wall temperatures defined on both solid and fluid boundaries. For the inlet turbulence, the turbulence intensity and eddy viscosity ratio are defined as 5% and 10, respectively.

For the EWF model, the momentum equation is solved with gravity force. The phase change between water liquid and vapor is driven by the wall boundary layer model, with built-in vapor saturation pressure being used. The film's maximum thickness is set as 0.005 m. The Second Order Implicit scheme is used for temporal discretization, while the Second Order Upwind scheme is used for continuity, momentum, and energy equations. The adaptive time-stepping approach is used, with a maximum Courant number of 0.2 for coarse meshes A-C, which is reduced to 0.05 for finer meshes of D and E for better solution convergence. The initial time step is defined as 1×10-5 s, with an increase factor of 1.5 and a decrease factor of 2. More information about the implemented EWF model can be found in Ref. [10].

4.5. Results and Discussion

The first simulation task compares the condensate mass flow rates of all five cases in Table 4 across all five meshes. As shown in Fig. 6, for all meshes, the magnitude of condensate mass flow rate increases from Cases 1 – 3, before dropping for Case 4 and increasing again for Case 5. This trend slightly differs from the measurements [2], where the condensate mass flow rate monotonically increases from Case 1 to Case 5. It is also noted that the solution will converge at Mesh 4, meaning a further refinement beyond Mesh 4 is unnecessary.

For the surface heat flux on the aluminium wall, which is adjacent to the primary test channel, the simulated results along the channel axial coordinate have been compared in Figs. 8 - 12 across all the five meshes. For all five simulation cases, the solutions match closely to the experimental data in both magnitude and trends, showing the surface heat flux continuously drops as the air/vapor mixture flows downstream and is being heated up. Similar to the condensate mass flow rate (see Fig. 6), the surface heat flux will converge on Mesh 4. For both variables, the simulation accuracy is generally satisfactory.

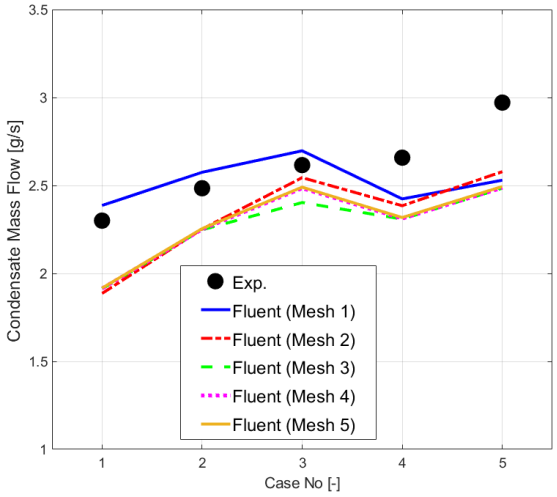

Figure 6. Condensate mass flow rates for all five cases across five meshes. Experimental data (circles) taken from Ref. [2].

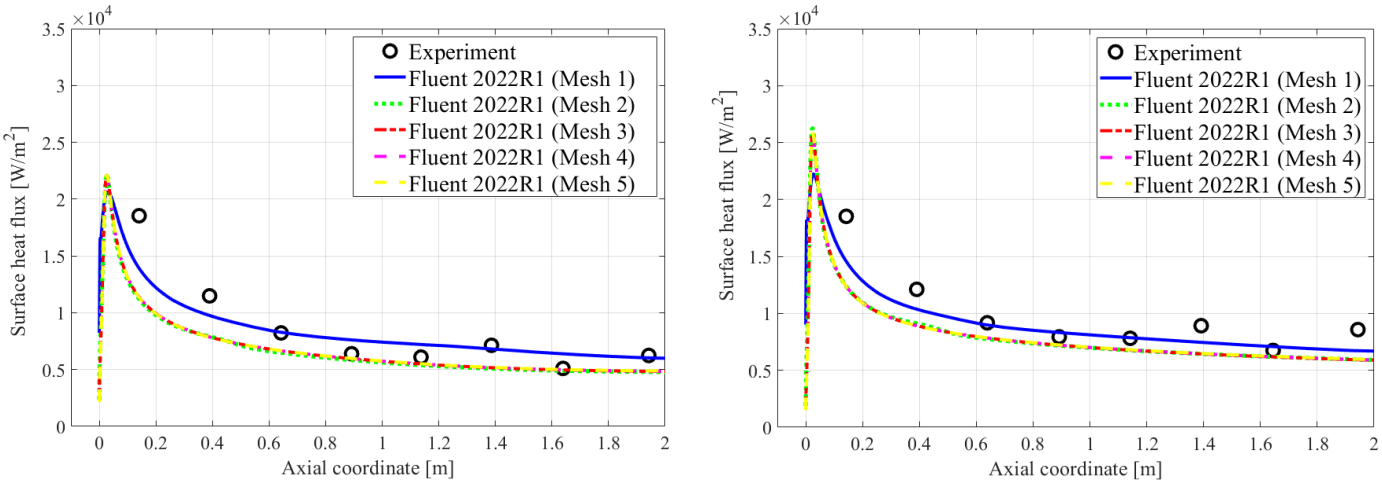

(a) (b)

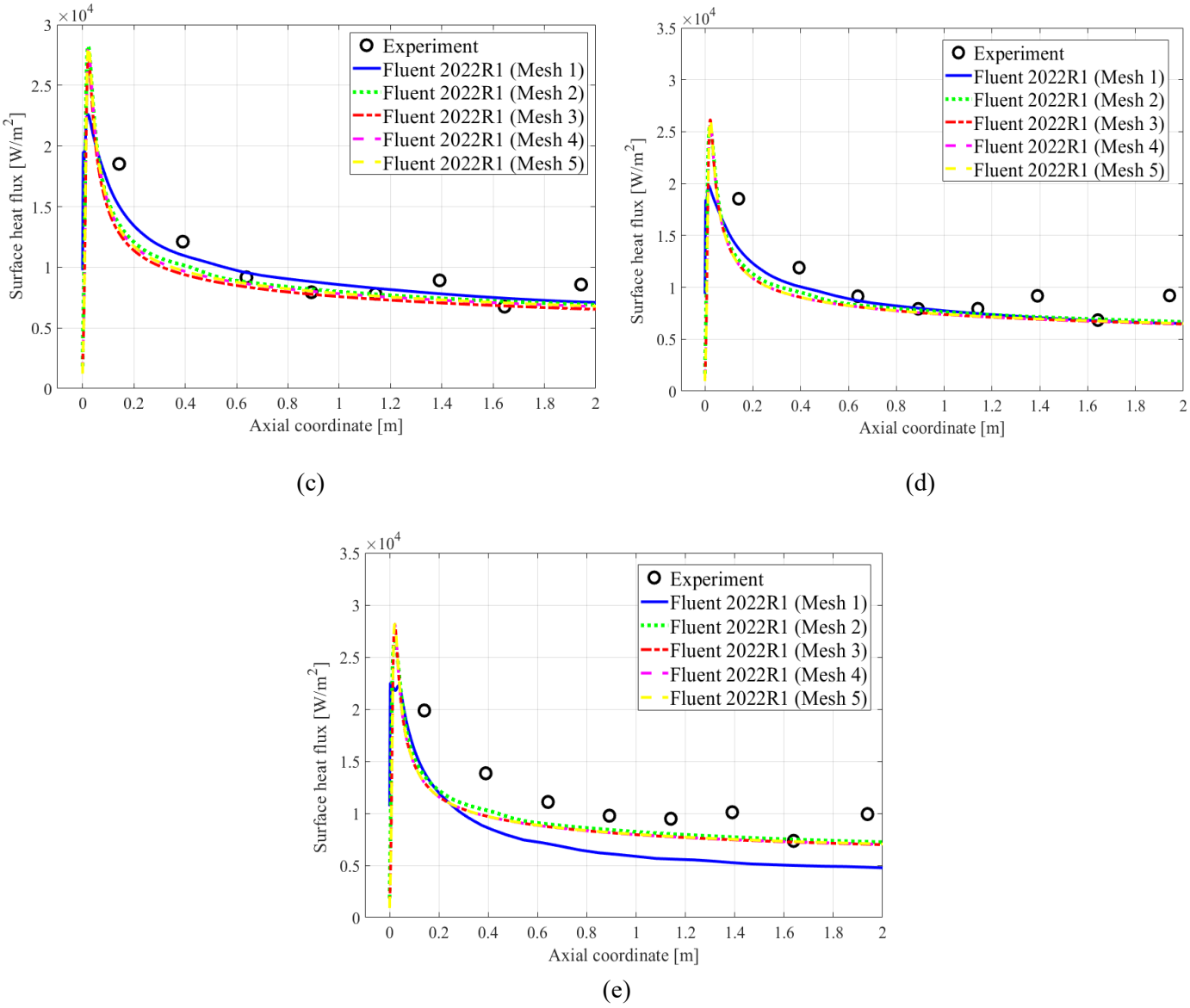

Figure 7. Surface heat flux for (a) Case P10-T30-V15; (b) Case P10-T30-V20; (c) Case P10-T30-V25; (d) Case P10-T30-V30; (e) Case P10-T30-V35 over all five meshes. Experimental data (circles) taken from Ref. [2].

5. Conclusions

The Eulerian Wall Film (EWF) model, along with the wall boundary layer phase change approach, for modelling concentration driven evaporation and condensation phenomena have been introduced in this paper. The EWF model has been validated by simulating two laboratory cases: the first case refers to an evaporation experiment by Du et al. [1], and the second case refers to the CONAN condensation experiments performed by Ambrosini et al. [2]. For both cases, the EWF model can accurately predict the surface heat flux and the evaporation (or condensate) mass flow rates on the wall. The EWF model is also able to capture the development of film thickness and temperature profile along the walls. The film phase change rates have also been well captured by the new wall boundary layer evaporation and condensation model, which does

not require any calibration of the phase change coefficients which is contrary to the model utilized by Du et al. [1]. Discretization errors and mesh sensitivity were studied for the CONAN case. For the assumed turbulence boundary conditions at the inlet, the condensation rate and surface heat flux follow the trend of the experimental data well, but the present model under-predicts their values under high wet air mass flow rates. The results on the coarse mesh with respect to the condensation rate seems to agree best with the experimental data but shows the highest deviation when compared to measured surface heat flux profile. This behaviour will be investigated in future work. Finally, the developed workflow and best practice settings for wall film modelling by this work can be applied to more complex applications in nuclear and automotive industries.

References

[1] P. Hu, K. Du, S. Zhai, and Y. Yang, “Experiment study of water film/air counter-current flow heat transfer on a vertical plate for passive containment cooling system,” Nuclear Engineering and Design, vol. 328, pp. 73–79, 2018.

[2] W. Ambrosini, N. Forgione, F. Oriolo, C. Dannoehl, and HJ Konle. “Experiments and CFD analyses on condensation heat transfer in a square cross section channel,” in Proceedings of the 11th International Topical Meeting on Nuclear Reactor Thermal Hydraulics (NURETH-11), Avignon, France, 2005.

[3] M. Zheng, J. Yan, S. Jun, L. Tian, X. Wang, and Z. Qiu, “The general design and technology innovations of CAP1400,” Engineering, vol. 2, no. 1, pp. 97–102, 2016.

[4] W. Ambrosini, A. Manfredini, F. Mariotti, F. Oriolo, and P. Vigni, “Heat transfer from a plate cooled by a water film with countercurrent air flow,” Nuclear Technology, vol. 112, no. 2, pp. 227–237, 1995.

[5] X. Wang, H. Chang, M. Corradini, T. Cong, and J. Wang, “Prediction of falling film evaporation on the AP1000 passive containment cooling system using ANSYS FLUENT code,” Annals of Nuclear Energy, vol. 95, pp. 168–175, 2016.

[6] D.C. Wilcox, Turbulence Modeling for CFD, DCW Industries, Second Edition, 1998.

[7] S.B. Pope, Turbulent Flows, Cambridge University Press, 2000.

[8] J. Xiao, J. Travis, and M. Bottoni, “Status of dynamic water film model development in 3-D CFD code GASFLOW-MPI for analysis of passive containment cooling system,” Annals of Nuclear Energy, vol. 108, pp. 99–112, 2017.

[9] H. Hong, H. T. Kim, and C. K. Moon, “Numerical analysis of heat transfer phenomena when mitigating severe accident with external reactor vessel flooding,” in Proceedings of the of the 20th International Conference on Nuclear Engineering and the ASME 2012 Power Conference, Anaheim, CA, USA, July 2012.

[10] Ansys Inc., Ansys Fluent Theory Guide 2022R2, Canonsburg, PA, USA, 2022.

[11] Zschaeck, G., T. Frank, and A. D. Burns. "CFD modelling and validation of wall condensation in the presence of non-condensable gases," Nuclear Engineering and Design, vol. 279, pp. 137-146, 2014.

[12] T. E. Springer, T. A. Zawodzinski, and S. Gottesfeld. "Polymer Electrolyte Fuel Cell Model". J. Electrochemical Soc., vol. 138, no. 8, 1991.

[13] Kashuai Du, Po Hu, Zhen Hu, "Numerical Investigation of water film evaporation with the counter current air in the asymmetric heating rectangular channel for passive containment cooling system", Science and Technology of Nuclear Installations, vol. 2020, 2020.

[14] W. Ambrosini, M. Bucci, N. Forgione, F. Oriolo, S. Paci, Quick Look on SARnet Condensation Benchmark-1 Results, University of Pisa, Step 1 - 10 kW Heating Power Exercise, Pisa, Italy, 2008.